Perovskite-like K_3TiOF_5 Exhibits (3+1)-Dimensional Commensurate Structure Induced by Octahedrally Coordinated Potassium Ions

Fenghua Ding[†,1], Nenian Charles[‡,1], Jaye K. Harada[‡], Christos D. Malliakas[†], Chi Zhang[‡], Roberto dos Reis[‡], Kent J. Griffith[†], Matthew L. Nisbet[†], Weiguo Zhang[§], P. Shiv Halasyamani[§], Vinayak P. Dravid[‡], James M. Rondinelli[*,‡], and Kenneth R. Poeppelmeier[*,†]

[†] Department of Chemistry, Northwestern University, Evanston, IL 60208, USA

[‡] Department of Materials Science and Engineering, Northwestern University, Evanston, IL 60208, USA

[§] Department of Chemistry, University of Houston, Houston, Texas 77204, USA

ABSTRACT: The elpasolite and cryolite type oxyfluorides can be regarded as superstructures of perovskite and exhibit structural diversity. While maintaining a similar structural topology with the prototype structures, changes in the size, electronegativity, charge of cation and/or anion inevitably leads to structural evolution. Therefore, the nominal one-to-one relation suggested by a doubled formula of perovskite does not guarantee a simple twofold superstructure for many cases. Herein, the commensurately modulated perovskite-like K_3TiOF_5 was refined at 100 K from single crystal X-ray diffraction data using a pseudo-tetragonal subcell with lattice parameters of $a = b = 6.066(2)$ Å and $c = 8.628(2)$ Å. The length of the modulation vector was refined to $0.3a^* + 0.1b^* + 0.25c^*$. In the commensurate supercell of K_3TiOF_5, the Ti^{4+} and K^+ cations in $[TiOF_5]^{3-}$ and $[KOF_5]^{6-}$ octahedral units were found to be significantly displaced from the average atomic positions refined in the subcell. The displacements of the K^+ cations are ±0.76 Å and those for the Ti^{4+} cations are approximately ±0.13 Å. One- and two-dimensional solid-state ^{19}F NMR measurements revealed two tightly clustered groups of resonances in a ratio of *ca.* 4:1, assigned to equatorial and axial fluorine, respectively, consistent with local $[TiOF_5]^{3-}$ units. S/TEM results confirmed the average structure. Electronic structure calculations of the idealized *I4mm* subcell indicate the instability to a modulated structure arises from soft acoustic and optical modes, consistent with an elasticity instability in the stiffness tensor.

Introduction

The study of oxyfluoride perovskites began with Linus Pauling's investigation of $(NH_4)_3MoO_3F_3$ in 1920.[1] He found that deciphering the arrangement of the $[MoO_3F_3]^{3-}$ group, including assessing whether the oxide and fluoride ions exhibited long-range order, complicated the solution of the crystal structure. This observation ultimately led to the conclusion that $(NH_4)_3MoO_3F_3$ exhibited a distorted crystal structure and the oxide and fluoride ions formed a solid solution. Since then, oxyfluoride perovskites have remained of keen interest for their peculiar crystal chemistry and prospect for noncentrosymmetry.[2-4] Investigations that followed ultimately revealed that the $[MO_xF_{6-x}]^{n-}$ heteroleptic units in these perovskites exhibit local anion order. Weak interactions, however, among neighboring anionic groups leads to long-range orientational disorder. Although demonstrable control over anionic order remains an open challenge, achieving it has the potential to transform the design of functional materials.[5,6] The careful examination of this structural space using state-of-the-art synthetic and characterization techniques is critical to advancing crystal-chemical principles for anionic control.

The evolution of structural characterization in the cryolite $A_3MoO_3F_3$ (A = Na, K, Rb) family of compounds underscores the importance of reassessing our understanding of oxyfluoride compounds. Early work showed that most members of this family were susceptible to coupled ferroelastic–ferroelectric displacive phase transitions upon cooling from high temperature.[7-11] However, details of the crystal structures were largely unknown, making it difficult to discern their ferroelectric mechanism. Interestingly, a detailed reassessment of $Na_3MoO_3F_3$ using X-ray, electron, and neutron diffraction revealed that the small radius of the Na^+ ion produces significant under-bonding to induce large octahedral rotations.[12] The result is a metrically rhombohedral structure, compa-

rable to $LiNbO_3$, with oxide and fluoride ions ordered in a *fac*-orientation on the $[MoO_3F_3]^{3-}$ units. This observation motivated Woodward *et al.* to substitute soft Ag^+ ions for hard Na^+ in $Ag_{1.5}Na_{1.5}MO_3F_3$ (M = Mo, W) to investigate how the differences in bonding preferences of the cations surrounding the oxyfluoride anionic groups would influence the orientation of the octahedra.[13] The authors observed that both chemistries crystallized in structures related to $LiNbO_3$ and $Na_3MoO_3F_3$. Moreover, the anionic groups adopted orientations with a preference for Ag^+ ions bonded to the oxide anions and Na^+ ions bonded to the fluoride anions. A recent synchrotron and neutron powder diffraction study of related $[MoO_3F_3]^{3-}$ compounds with larger K^+ and Rb^+ cations revealed the absence of orientational disorder with increasing *A*-site-cation size in the presence of noncooperative octahedral tilting.[14]

K_3TiOF_5 is a 3*d* transition metal oxyfluoride analogue of $Na_3MoO_3F_3$, however, the transition-metal–oxide ligand interaction is less covalent and the heteroleptic octahedra are likely more susceptible to orientational disorder since only one in six ligands are oxygen. These features make it an ideal material to better understand the role of counter-cation–ligand bonding preferences on the $[TiOF_5]^{3-}$ orientational order. The metric shape of the cell has been indexed as a tetragonal unit cell at ambient conditions ($a = b$ = 6.102 Å, c = 8.655 Å).[15,16-18] However, we are unaware of any studies that refine the space group symmetry, internal ion coordinates, or assess whether K_3TiOF_5 is inversion symmetric. For the measured lattice constants there are three simple arrangements of the ions consistent with the cryolite structure (**Figure 1**). Without long-range ordering of the oxide and fluoride ions (solid solution), K_3TiOF_5 should crystallize with *I*4/*mmm* symmetry (**Figure 1a**). However, with long-range ordering of the anionic sublattice, K_3TiOF_5 could exhibit either a centrosymmetric *P*4/*nmm* (**Figure 1b**) or a noncentrosymmetric *I*4*mm* (**Figure 1c**) symmetry. Interestingly, a combination of X-ray diffraction, polarizing microscopy and microcalorimetry experiments demonstrated that similar to the $A_3MoO_3F_3$ family, K_3TiOF_5 undergoes a reversible phase transition between a cubic centrosymmetric phase and a ferroelectric/ferroelastic phase around 490 K, which suggests that the *I*4*mm* structure is the most plausible ground state.[18]

Contrary to the aforementioned simpler models, we show that the low temperature structure of K_3TiOF_5 adopts a perovskite-like (3+1)-dimensional commensurate structure, which is solved from single-crystal X-ray diffraction data. ^{19}F solid-state NMR and optical spectroscopy measurements suggest that ordered octahedral $[TiOF_5]^{3-}$ heteroleptic units comprise the structure. S/TEM imaging, supported by density functional theory (DFT) calculations, are consistent with the average structure in *I*4*mm*. Calculated phonon dispersions of the average *I*4*mm* structure do not show the expected commensurate modulation, suggesting that the high-temperature structure is not *I*4*mm* or there is a significant order-disorder component to the complex phase transition.

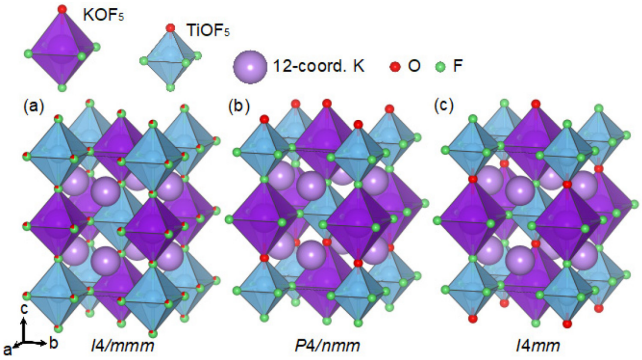

Figure 1. Metrically tetragonal unit cells consistent with the K_3TiOF_5 cryolite chemistry and prior $a = b$ = 6.102 Å, c = 8.655 Å measurements. (a) Centrosymmetric anion-disordered *I*4/*mmm*, (b) centrosymmetric anion-ordered *P*4/*nmm*, and (c) noncentrosymmetric anion-ordered *I*4*mm* crystal structure models.

Experimental Section

Caution: Hydrofluoric acid is toxic and corrosive! It must be handled with extreme caution and the appropriate protective equipment and training.

Reagents. Potassium fluoride (KF, 99.0%), Titanium dioxide (TiO_2, 99.0%), and hydrofluoric acid (49.0% HF_{aq} by weight) were used as received from Sigma-Aldrich. Deionized (DI) water was used in the synthesis.

Infrared (IR) Spectroscopy. The Fourier transform infrared (FTIR) spectrum in the range from 600 cm^{-1} to 3000 cm^{-1} was recorded on a Bruker 37 Tensor FTIR spectrometer at room temperature.

Raman Spectroscopy. The Raman spectra were collected on a Horiba LabRAM HR Evolution Confocal Raman System equipped. A solid-state laser (532 nm) was used as the excitation source.

Thermal Analysis. Differential thermal analysis (DTA) was carried out with a Netzsch STA 449 F3 Jupiter Simultaneous Thermal Analysis instrument. Crystalline samples were placed in gold crucibles to avoid reaction between sample and container and then inside an aluminum crucible and heated from room temperature to 870 °C at a rate of 10 °C/min. The samples were then cooled to room temperature at the same rate under flowing helium with a flow rate of 25 mL/min. The DTA curve exhibits a clear endothermic peak beginning around 770 °C that reaches a maximum at approximately 820 °C (**Figure S1** in Supporting Information).

Second-Order NLO Measurements. Second-harmonic generation (SHG) measurements of polycrystalline samples were performed with a Nd:YAG laser (λ = 1064 nm) as the incident light source. Samples of the title compound were ground and sieved into seven distinct size ranges for the test. Ground α-SiO_2 powder was used as a reference and sieved into the same size ranges. The intensities of the frequency-doubled output emitted from the samples were detected by a photomultiplier tube.

Solid-state Nuclear Magnetic Resonance (NMR) Spectroscopy. Magic angle spinning (MAS) ^{19}F NMR spectra of K_3TiOF_5 were recorded in a static magnetic field of 9.4 T with a Bruker Avance III spectrometer. The finely ground polycrystalline sample was loaded into a 1.6 mm diameter zirconia rotor (internal volume = 8 μL) with Torlon caps. Unless otherwise noted, spectra were measured at 38 kHz MAS in a Phoenix narrow-bore 1.6 mm HFX probe. ^{19}F spectra were measured with a rotor-synchronized Hahn-echo (π/2–τ–π–τ–acquire) pulse sequence using a 90° RF pulse of 1.80 μs. T_1 (spin–lattice) relaxation was measured with a saturation-recovery pulse sequence. The recycle delay of the echo spectra was 5 s, which was greater than $5T_1$ (for the longest T_1) at all temperatures. The chemical shifts were externally referenced to the center of the doublet in $NaPF_6$ (at 39 kHz) at –82.5 ppm. In the absence of applied heating or cooling, frictional heating at 38 kHz MAS led to an internal sample temperature of 42 °C. Variable-temperature spectra were collected from –13 to 72 °C with a Bruker Cooling Unit and nominal temperature stability of ±0.5 °C. Sample temperatures were externally calibrated via the temperature-dependent ^{207}Pb shift of lead nitrate.[19,20] Two-dimensional homonuclear spin-exchange spectra were recorded with a $\pi/2$–t_1–$\pi/2$–τ_m–acquire pulse sequence. The mixing time (τ_m) was varied from 100 μs to 200 ms. The recycle delay of the 2D spectra was 1.5 s, corresponding to about $2T_1$; 16 scans were collected in F_2 and 720 scans were collected in F_1. The measurement time was approximately 5 h for each 2D spectrum.

Scanning and Transmission Electron Microscopy. Polycrystalline products were crushed to powders and dropped on ultrathin C-coated Mo grids. Selected area electron diffraction patterns (SAED), bright-field transmission electron microscopy imaging (BF-TEM), and high-resolution electron microscopy imaging (HREM) were obtained using a JEOL Grand ARM operated at 300 kV at using LN_2 holder to lower the sample temperature to 100K to preserve the structure integrity. Atomic resolution high-angle annular dark-field (HAADF) images (in scanning transmission electron microscopy were acquired using a C_s-corrected JEOL ARM 200CF operated at 60 kV at room temperature, using convergence angle of 21.6mrad and collection angle of 90–200 mrad.

Preparation of K_3TiOF_5. Initially, the precursor compound K_2TiF_6 was synthesized by the reaction of 0.04 mol of TiO_2 (3.2 g) and 0.08 mol of KF (4.64 g) through hydrothermal synthesis with 6 ml of 49% HF_{aq} in a 125 ml Teflon-lined Parr pressure vessel filled with 40 ml of deionized H_2O as backfill. Pressure vessels were heated to 200 °C for 48 h followed by cooling to room temperature with a rate of 0.1 °C/min. The Teflon-lined Parr was then left undisturbed at room temperature for another 48 h to allow crystallization. The K_2TiF_6 precursor was finally recovered via vacuum filtration and vacuum drying for subsequent synthesis.

Crystalline samples of K_3TiOF_5 were prepared via a high temperature solid-state method with a stoichiometric ratio of K_2TiF_6 (1.046 g), KF (1.012 g), and TiO_2 (0.342 g). The reagents were ground together in an agate mortar and pestle and pressed into a cylindrical sample. The sample preparation was operated in glovebox due to the hygroscopic nature of KF. The sample was then placed in a platinum crucible and inserted into a tube furnace under flowing Argon gas. The furnace was pre-equilibrated for 8 h to remove air and then heated to 790 °C at a rate of 5 °C/min and held at this temperature for 20 h. The furnace was cooled to 600 °C at a rate of 0.1 °C/min and then cooled to room temperature naturally. Colorless crystals were obtained (**Figure S2**), and their purity was confirmed by powder X-ray diffraction (**Figure S3**). The signature extra peaks and split peaks in the experimental PXRD pattern of K_3TiOF_5 are indicative of the commensurate structure.

Structure Solution and Refinement Methods. A colorless and transparent blocky crystal of K_3TiOF_5 with dimensions of 0.12 × 0.08 × 0.06 mm^3 was chosen for structure determination. Single-crystal X-ray diffraction data for K_3TiOF_5 at 100 K were collected with the use of an XtaLAB Synergy diffractometer equipped with a micro-focus sealed X-ray tube PhotonJet (Mo) X-ray source and a Hybrid Pixel Array Detector (HyPix) detector. The crystal-to-detector distance was 5.00 cm and data were collected by a scan of 0.5° in ω and φ settings. The exposure time was 20 s/frame. The collection of intensity data as well as cell refinement and data reduction were carried out with the use of the CrysAlisPro software. Absorption corrections, as well as incident beam and decay corrections, were performed with the use of the program SADABS[21] for the subcell structure. The subcell structure was solved with the direct-methods program SHELXS and refined with the least-squares program SHELXL.[22] The final refinement included anisotropic displacement parameters.

An multi-scan absorption correction was performed (CrysAlisPro) and the modulated structure was refined with JANA2006.[23] Atomic coordinates of the atoms in the subcell and initial values of their modulation functions were determined by the charge-flipping method.[24,25] The anion positions were refined without differentiating between oxygen and fluorine, owing to their similar X-ray atomic scattering factors. The distortion (positional or displacement parameter) of a given atomic parameter x_4 in the subcell was expressed by a periodic modulation function $p(x_4)$ in the form of a Fourier expansion (eq. 1):

$$p(k+x_4) = \sum_{n=1}^{m} A_{sn} \sin\left[2\pi\overline{q}_n(k+x_4)\right] + \sum_{n=1}^{m} A_{cn} \cos\left[2\pi\overline{q}_n(k+x_4)\right]$$

where A_{sn} is the sinusoidal coefficient of the given Fourier term, A_{cn} is the cosine coefficient, n is the number of modulation waves used for the refinement, and k is the lattice translation. $\overline{q}_n = \sum_{i=1}^{d} \alpha_{ni} q_i$ where α_{ni} are integer numbers for the linear combination of the commensurate modulation vectors q_i. A useful coordinate t, which characterizes and describes the real three-dimensional (3D) structure and constructed as a perpendicular intersection with the fourth dimensional axis, is defined as $t = x_4 - \mathbf{q} \cdot \mathbf{r}$ where $\mathbf{r}$ is a vector in the real 3D reciprocal space.

Satellite reflections of eight orders were observed and used for the refinement. Consequently, eight modulation waves for positional and thermal displacement parameters were used for all atoms. Refinement of the modulation parameters for the Ti occupancy factors gave negligible improvement of the overall agreement factor. Therefore, modulation parameters for the occupancy factors were not included in the final refinement. Only the symmetry-allowed Fourier terms were refined.

Calculation Details. Density functional theory (DFT) calculations were performed as implemented in the Vienna Ab Initio Simulation Package (VASP).[26, 27] The generalized gradient approximation (GGA) of Perdew–Burke–Ernzerhof revised for solids (PBEsol)[28] was used, as recommended for oxyfluoride materials.[29] A 650 eV plane wave cutoff and the projector augmented wave (PAW) method[30] were used to treat the core and valence electrons using the following valence configurations: $3s^2 3p^6 4s^1$ for K, $3d^3 4s^1$ for Ti, $2s^2 2p^4$ for O, and $2s^2 2p^5$ for F. Monkhorst–Pack *k*-point meshes[31] of various densities were used and were at a minimum converged to achieve energy differences of less than 5 meV per atom. Gaussian smearing (10 meV width) was used for Brillouin zone (BZ) integrations. Structural relaxations were performed until the Hellmann–Feynman forces were less than 1 meV $Å^{-1}$ on each atom and total energies were less than 10^{-8} eV. Phonon calculations were performed using the finite displacement method as implemented in the PHONOPY package.[32] Symmetry analyses of superspace groups and single commensurate modulations was facilitated with the ISO(3+1)D software.[33, 34]

Results and Discussion

X-ray diffraction of K_3TiOF_5

From single crystal X-ray diffraction intensity data, a complex commensurate supercell was identified (**Figure 2**). The basic structure (subcell) used for the description of the K_3TiOF_5 supercell consists of a unit cell with lattice constants of $a = b = 6.066$ (2) Å, and $c = 8.654(4)$ Å. The length of the modulation vector was refined to $0.3a^* + 0.1b^* + 0.25c^*$. A total of 311384 reflections (28208 main + 283176 supercell) were collected at 100 K (**Table 1**). Due

Table 1. Crystal Data and Structure Refinement for K_3TiOF_5.

Empirical formula	K_3TiOF_5
Formula weight	276.2
Temperature	100.00(18) K
Wavelength	0.71073 Å
Crystal system	triclinic
Space group	$P1(\alpha\beta\gamma)0$
Unit cell dimensions	$a = 6.0665(2)$ Å, $\alpha = 90.005(2)°$ $b = 6.0658(2)$ Å, $\beta = 90.006(2)°$ $c = 8.6285(2)$ Å, $\gamma = 89.991(2)°$
q-vector(1)	$0.3a^* + 0.1b^* + 0.25c^*$
Volume	317.513(17) $Å^3$
Z	2
Density (calculated)	2.8886 g/cm^3
Absorption coefficient	3.338 mm^{-1}
F(000)	264
Crystal size	0.12 x 0.08 x 0.06 mm^3
θ range for data collection	2.06 to 38.28°
Index ranges	$-11 \le h \le 11$, $-10 \le k \le 10$, $-15 \le l \le 15$, $-8 \le m \le 8$
Reflections collected	311384 (28208 main + 283176 satellites)
Independent reflections	32293 (9526 main + 98773 satellites) [$R_{int} = 0.0363$]
Completeness to $\theta = 27.69°$	96%
Refinement method	Full-matrix least-squares on F^2
Data / constraints / restraints / parameters	32293 / 4 / 0 / 3061
Goodness-of-fit on F^2	3.07
Final R indices [$I>3\sigma(I)$]	$R_{obs} = 0.0855$, $wR_{obs} = 0.1718$
R indices [all data]	$R_{all} = 0.1366$, $wR_{all} = 0.1991$
Final R main indices [$I>3\sigma(I)$]	$R_{obs} = 0.0875$, $wR_{obs} = 0.1745$
R main indices (all data)	$R_{all} = 0.1501$, $wR_{all} = 0.2083$
Final R 1st order satellites [$I>3\sigma(I)$]	$R_{obs} = 0.0770$, $wR_{obs} = 0.1603$
R 1st order satellites (all data)	$R_{all} = 0.1116$, $wR_{all} = 0.1808$
T_{min} and T_{max} coefficients	0.9338 and 1.0000
Largest diff. peak and hole	2.13 and −1.45 e·$Å^{-3}$

$R = \Sigma||F_o| - |F_c|| / \Sigma|F_o|$, $wR = (\Sigma[w(|F_o|^2 - |F_c|^2)^2] / \Sigma[w(|F_o|^4)])^{1/2}$ and $w=1/(\sigma^2(I)+0.0004I^2)$

to the diagonal direction of the modulation vector along all three directions in the unit cell, the only acceptable crystal system is triclinic. To conclusively distinguish between the noncentrosymmetric $P1$ and centrosymmetric $P\bar{1}$ triclinic space groups, we measured the non-linear optical (NLO) response of K_3TiOF_5 (~0.5×SiO_2),

which is nonzero for crystals with broken inversion symmetry (see **Figure S4**).

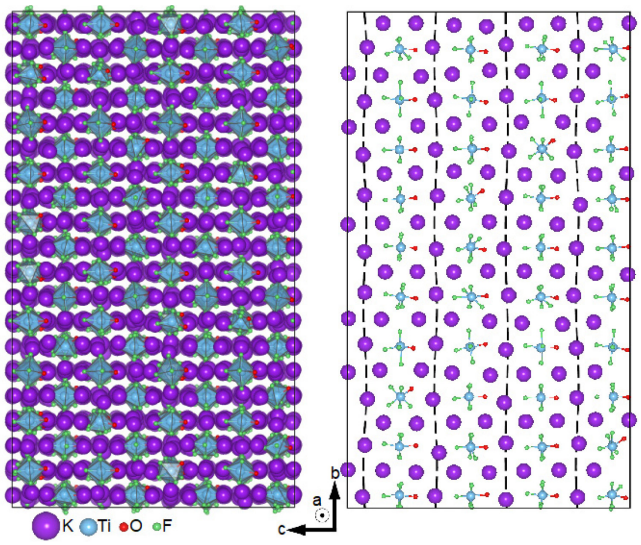

Figure 2. Commensurate structure of K_3TiOF_5 as solved from single crystal X-ray diffraction data. (left) Full structure model and (right) a (100) plane of atoms. The dashed lines serve as guides to the eye to view the K^+ displacements that occur in (011) planes.

The intensity of the supercell reflections was much weaker than the intensity of the subcell reflections (see **Figure 3a**). Given the small contrast of the atomic structure factors between oxygen and fluorine, ^{19}F NMR spectroscopy was used to directly probe the number of fluorine sites and their local crystallographic environment.[35-37] The spectra are consistent with a local ratio of O:F =1:5 in each TiL_6 (L = O, F) octahedra (see the following ^{19}F NMR discussion). This is also supported by charge balance considerations of the compound. Furthermore, considering the non-centrosymmetric character of the structure, a parallel configuration of two $[TiOF_5]^{3-}$ octahedra was chosen in the subcell for the refinement (see **Figure 3b**). The subcell structure consists of six unique K^+ ions, two unique Ti^{4+}, ten unique F^-, and two unique O^{2-} in the asymmetric unit (**Figure 3b**). The atomic coordinates, occupancies, and equivalent isotropic displacement parameters for K_3TiOF_5 are tabulated in **Table S1**. Due to the modulation, the $[TiOF_5]^{3-}$ and $[KOF_5]^{6-}$ octahedra were found to be significantly displaced from their average atomic positions as refined in the subcell. The displacement of these *B*-site K^+ ions is ±0.76 Å and for the Ti^{4+} ions ±0.13 Å. In comparison, the displacements of those *A*-site K^+ ions are relatively smaller (Figure 3c). The displacements do not occur along the principal axes of the crystal; however, we present representative projections of the displacements along the *a*-axis and the modulation direction in **Figures 3c** and **3d**. The Fourier components of the displacive modulation for K_3TiOF_5 are tabulated in Table S1 in the Supporting Information (SI). The commensurate modulation of the double perovskite structure modifies the positions of all atoms in K_3TiOF_5. As the $[TiOF_5]^{3-}$ and $[KOF_5]^{6-}$ octahedra (*i.e.*, *B*-site K3 and K4) tilt, the coordination environments of the twelve-coordinate K ions (*A*-site K1, K2, K5, and K6, see **Figure S5** for their coordination environments) are also distorted. However, in the average structure, the out-of-center distortion of octahedrally coordinated Ti^{4+} and K^+ was small. The six bond lengths of Ti-O/F and K-O/F in each local $[TiOF_5]^{3-}$ and $[KOF_5]^{6-}$ octahedra were in the range of 1.761-1.807 Å, 1.739-1.794 Å, 2.537-2.623 Å, 2.520-2.635 Å, for Ti(1), Ti(2), K(3) and (K4), respectively (Fig. 3b). Therefore, K_3TiOF_5 possesses mild SHG response (~0.5×SiO_2) despite of the polar character of the structure.

The out-of-center distortion has been often found around d^0 transition metals. The distortion increases with increasing formal charge and decreases with increasing size of the cation.[38] Ti^{4+} cation thus possesses easily-distorted character. In the crystal structures, the size of distortion was believed to be influenced by at least several factors, including electronic structure of the cation; the structure of the bond network; and lattice incommensurations (lattice stress).[38] The suppressed distortion $[TiOF_5]^{3-}$ octahedral is correlated with formation of the commensurate structure of K_3TiOF_5.

Electron diffraction of K_3TiOF_5

Based on the results of our experimental measurements thus far, the high symmetry structure of K_3TiOF_5 can be rationalized as belonging to the simplest commensurate approximate cell with pseudo-tetragonal lattice constants $a = b = 6.066(2)$ Å, $c = 8.628(2)$ Å and short-range oxide-fluoride ordering (**Table 1**). The anion-ordered structures consistent with the commensurate tetragonal lattice are centrosymmetric *P*4/*nmm* (No. 129) and polar *I*4*mm* (No. 107). The *P*4/*nmm* and *I*4*mm* structures (**Figure 1b and 1c**) can be viewed as counterparts where the acentric $[TiOF_5]^{3-}$ basic building units (with dipoles of ~6.84 Debye) are anti-aligned and aligned, respectively. From first-principles density functional theory (DFT) calculations, the polar *I*4*mm* structure is 13 meV lower in energy than the nonpolar *P*4/*nmm* counterpart.

Scanning/transmission electron microscopy (S/TEM) was leveraged to confirm the average structure of the subcell. Characterizing this compound with S/TEM is challenging due to sample sensitivity to the electron-beam energy and dose-rate and it can be quickly damaged via radiolysis or knock-on damage processes. To reduce structural damage by radiolysis, a liquid nitrogen (LN2) TEM sample-holder was used to stabilize the sample at approximately 100 K using acceleration voltage of 300kV. The STEM imaging was performed at room temperature, to avoid knock-on damage, the acceleration voltage was reduced to 60kV. Selected-area electron diffraction (SAED) patterns from K_3TiOF_5 along [021] and [111] zone axes and a convergent-beam electron diffraction pattern (CBED) along [001] were measured, confirming the average structure. As shown in **Figure 4**, the diffraction spots can be indexed using the *I*4*mm* structure. The forbidden spots of $(0\bar{1}2)$ and $(01\bar{2})$ in the diffraction pattern along the [021] zone axis match better with the simulated pattern of *I*4*mm* rather than *P*4/*nmm*, as shown in **Figure S6**, which is consistent with the DFT total energy calculations and the observed second-harmonic generation. No superlattice reflections corresponding to the commensurate modulation were observed in electron microscopy, which is probably because the sample is beam sensitive and long exposure times were not possible to enhance the

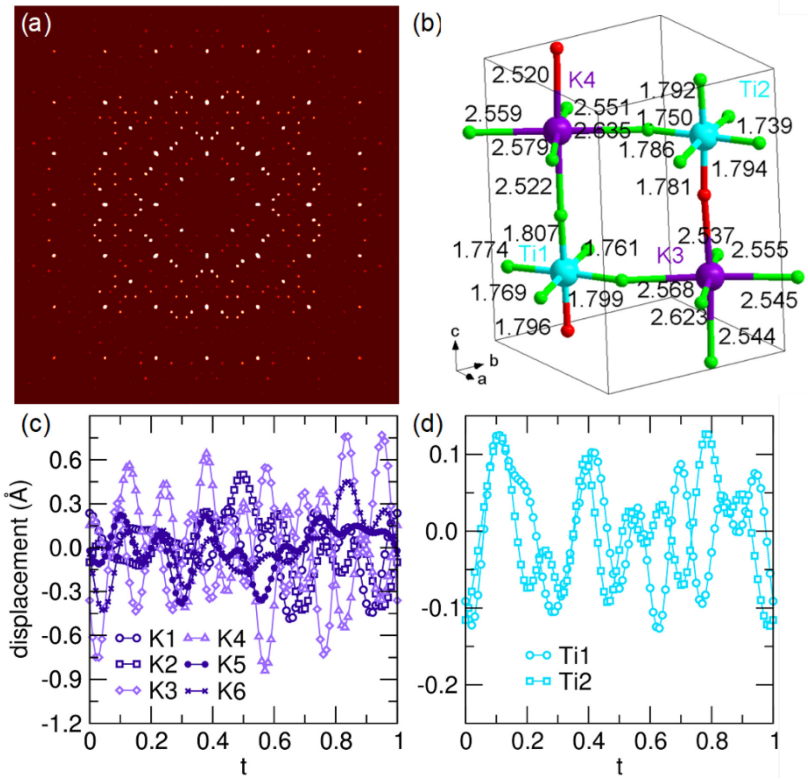

Figure 3. **(a)** Synthetic precession image of the 0*kl* layer of K_3TiOF_5 at 100 K. **(b)** The local octahedral environment of $[TiOF_5]^{3-}$ and $[KOF_5]^{6-}$ in the K_3TiOF_5 subcell. **(c)** *t*-plot of the atomic displacements of the K atoms along the *a*-axis as a function of modulation, and **(d)** *t*-plot of the atomic displacement of the symmetry generated Ti atoms along the *a*-axis as a function of modulation.

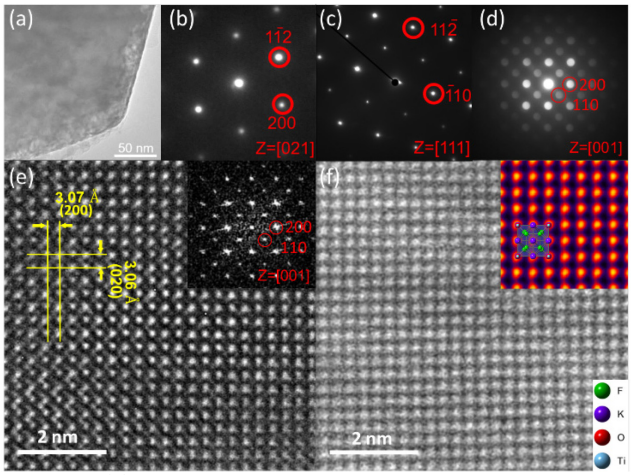

Figure 4. (a) Bright-field image of the single crystal particle of K_3TiOF_5. Selected-area electron diffraction patterns at the (b) [021] and (c) [111] zone axis. (d) Convergent-beam electron diffraction pattern along the [001] zone axis. The indices of reflections are based on the average structure of the subunit cell, space group *I*4*mm*. (e) HREM and (f) HAADF images along the [001] zone axis. Some lattice planes and their corresponding distances are marked in yellow in the HREM image. The upper right inset in (e) is the Fast Fourier transform (FFT) pattern of this area. Average unit cell calculated from the HAADF image and structure schematic overlaid.

brightness of these relatively low intensity spots. **Figure 4e** displays an HREM image along the [001] zone axis. The measured interplanar *d*-spacings of (200) are 3.07 Å, which are in good agreement with subunit cells. A HAADF-STEM image (**Figure 4f**) taken along the [001] zone axis provides a direct observation of atomic columns of the elements with a high atomic number (Z_K = 19 and Z_{Ti} = 22). The insets of **Figure 4f** show the theoretical subunit cell structure along the [001] direction and the average unit cell calculated from the HAADF image.

IR and Raman spectroscopy

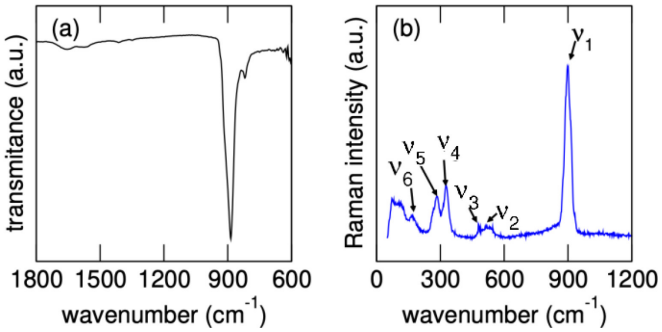

Figure 5. Vibrational properties of K_3TiOF_5 investigated using **(a)** mid-infrared absorption and **(b)** Raman spectroscopy.

An ideal heteroleptic $[TiOF_5]^{3-}$ octahedral unit is expected to have C_{4v} symmetry and exhibit a single Ti-O valence vibration.[39] Deviations in this expectation can be used to understand short- and long-range order in the crystal. The mid-infrared absorption spectra of K_3TiOF_5 shows a sharp characteristic peak at 885 cm^{-1} (**Figure 5a**), representing the internal vibration mode of Ti-O bond in the $[TiOF_5]$ structural unit. This $\nu_{Ti\text{-}O}$ vibrational frequency is reduced from the previously reported value ($\nu_{Ti\text{-}O}$=915 cm^{-1}).[15] The softening of the $\nu_{Ti\text{-}O}$ IR mode may be due to a weak interaction of *d-p* metal-oxide π orbital interaction in K_3TiOF_5 owing to the large displacement of Ti from the average position in the crystal structure.[40] The experimental Raman spectrum of K_3TiOF_5 at room temperature further supports the existence of short-range anion order within the $[TiOF_5]^{3-}$ units (**Figure 5b**). The intense line at the frequency of ν_1 (899 cm^{-1}) is consistent with the Ti-O stretching vibration of the $[TiOF_5]^{3-}$ unit observed in related oxyfluorides.[41,42] In addition, the lines of the Ti–F stretching and bending vibrations of the moiety occur at low frequencies (ν_2 = 519 cm^{-1}, ν_3 = 479 cm^{-1}, ν_4 = 326 cm^{-1}, ν_5 = 283 cm^{-1} and ν_6 = 167cm^{-1}).

Solid-state ^{19}F NMR spectroscopy

Due to the limited contrast between oxygen and fluorine in X-ray diffraction, the structure model refined from single crystal X-ray diffraction was insufficient to provide order/disorder information of oxygen and fluorine. Although IR and Raman spectra suggest the presence of Ti-O and Ti-F bonding environments, the nominal "K_3TiOF_5" formula and presence of $[TiOF_5]^{3-}$ octahedra require more robust confirmation. As a further probe of the local structure in K_3TiOF_5, a series of one- and two-dimensional solid-state ^{19}F NMR measurements was carried out. The ^{19}F spectrum under magic angle spinning (MAS) reveals two distinct resonance regions, each comprising several individual resonances (**Figure 6**). The region around –55 ppm is assigned to equatorial fluorine (relative to the oxygen) in $TiOF_5$ octahedra while the region centered near –135 ppm is assigned to axial fluorine. The lineshapes of the high and low frequency resonances can be deconvoluted with a minimum of four to five signals each, which represent lower limits on the number of local environments.

The assignment is made on the basis of the chemical shifts and peak intensities. Generally, fluorine sites in oxyfluoride octahedra that are *trans* to oxygen have longer M–F bond distances than those that are *trans* to other fluorine.[43] Longer bond distances translate to weaker paramagnetic shielding that arises from the orbital motion of the valence electrons on fluorine, according to Ramsey's theory of magnetic shielding.[44-46] Thus, the resonance from the axial fluorine atom in the $TiOF_5$ unit should appear at a lower frequency than the resonances from the equatorial fluorine atoms. An integral of 3.3:1 was observed for the high:low frequency resonances at –13 °C and 38 kHz MAS, the lowest temperature measured. The ratio decreased with increasing temperature or decreasing MAS rate (≤3.0 at 21 kHz/27 °C or 38 kHz/72 °C). A 4:1 ratio is expected for equatorial:axial fluorine atoms, but the rate and temperature dependence of the integral ratio suggest that the signals may be changing due to relaxation during the rotor-synchronized echo or due to broadening from chemical exchange. That both the high and low frequency signals comprise multiple individual resonances is consistent with the modulated structure model. It is interesting that distinct features are observed within each group of signals, rather than a broad distribution of fluorine sites, which suggests that the modulation may lead to discrete rather than continuous local environments in K_3TiOF_5.

Figure 6. ^{19}F NMR spectroscopy of K_3TiOF_5 at 38 kHz MAS and 9.4 T. (**a**) Variable-temperature spectra from –13 to 72 °C. (**b,c**) Detailed view of the two groups of isotropic resonances centered at

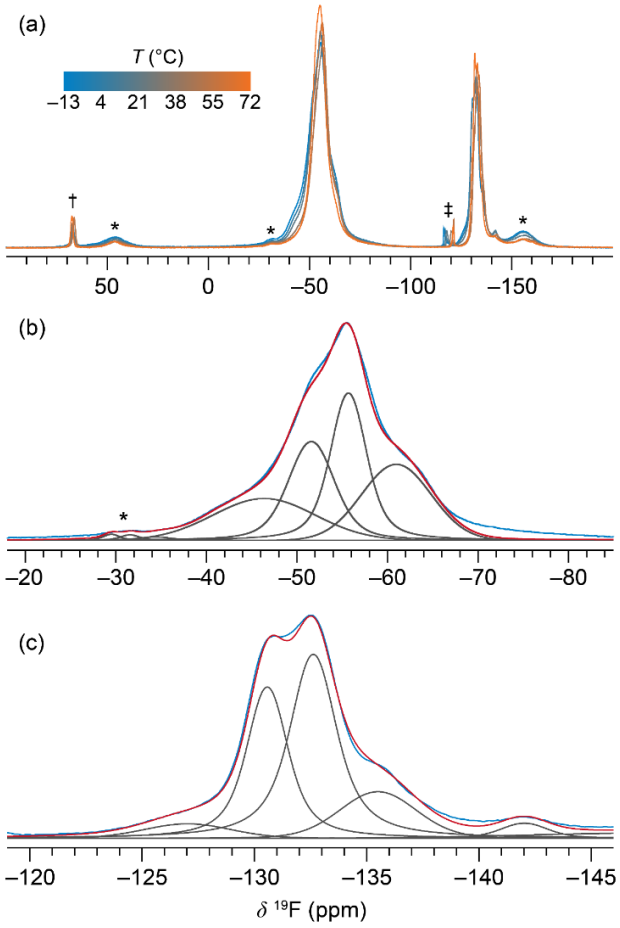

ca. (**b**) –55 ppm and (**c**) –135 ppm, assigned to equatorial and axial F sites in the $TiOF_5$ octahedra, respectively, at –13 °C. The groups of resonances in (**b**) and (**c**) could be fit reasonably well with four and five components, respectively. In (**b,c**), the experimental spectrum is shown in blue, the fit in red, and the individual components in gray. Spinning sidebands are denoted with asterisks, two small impurities are denoted with crosses. Relative intensities of the two groups of resonances can be observed in (**a**).

Figure 7. ^{19}F–^{19}F homonuclear correlation NMR spectroscopy of K_3TiOF_5 at 38 kHz MAS and 9.4 T. Spectra were recorded as a function of mixing time, shown in the top left of each panel. The

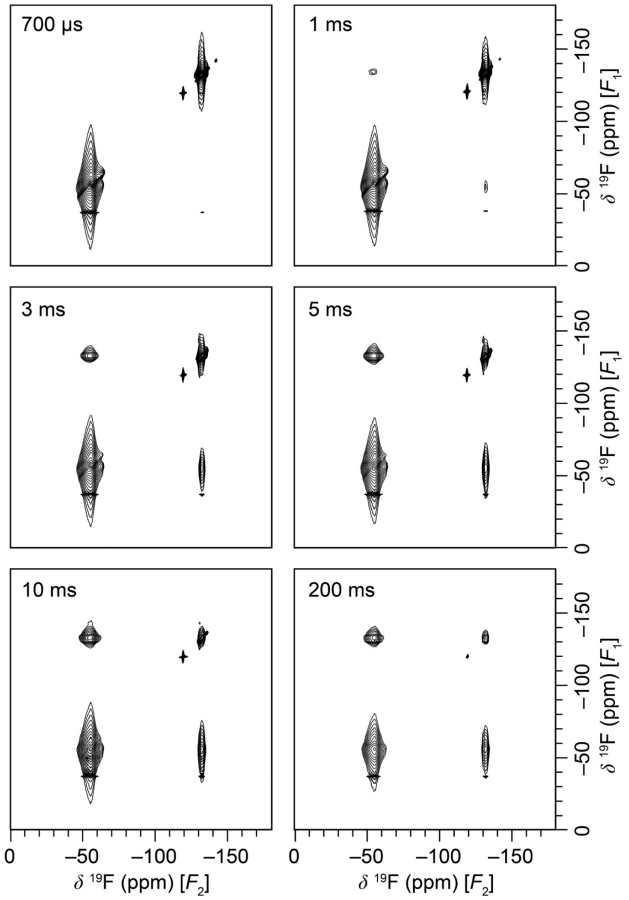

base level is set to 5% of the maximum intensity. The sample temperature was *ca.* 42 °C owing to frictional heating.

Spatial relationships between the fluorine sites were probed with two-dimensional dipolar-coupling-mediated ^{19}F–^{19}F correlation spectroscopy (**Figure 7**). Cross peaks were observed at short mixing times, appearing at 1 ms and nearly maximal by 3 ms. This result confirms that the two main sets of resonances are adjacent and is consistent with short interatomic distances between the axial and equatorial fluorine atoms along the edges of the $TiOF_5$ octahedra.

Origin of commensurate phase

Given that the commensurate phase could arise from symmetry-breaking displacive distortions, we analyzed the phonon dispersions of the average structure, *I*4*mm*, as determined by STEM imaging (**Figure 4**) to obtain further insight into its possible origin. Commensurate phases with large unit cells can arise from a softening of acoustic or optical phonon modes between high symmetry points. A group-theoretical analysis of a transition from the commensurate *I*4*mm* phase to a large triclinic (*P*1) commensurate phase suggests the phase transition is associated with an irreducible representation at the general point (GP) **k** = (a,b,c), which matches the form of our modulation vector.

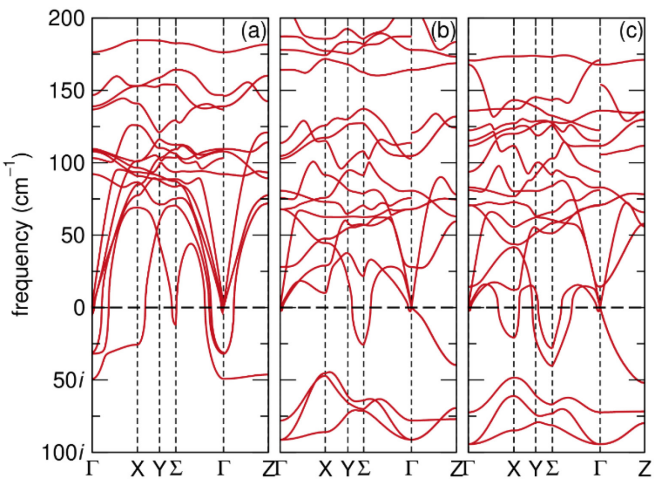

Figure 8. DFT computed phonon dispersions of **(a)** $K_2NaTiOF_5$ **(b)** K_3TiOF_5 and **(c)** $K_2RbTiOF_5$ in the *I*4*mm* structure with the non-analytical LO/TO correction included.

Thus, the instability driving the transition could be located anywhere in the Brillouin zone or proceed through a series of phase transitions, i,e., by first condensing a mode at **k** = (a,0,0), then **k** = (0,b,0), and so on.

Lattice dynamical calculations of *I*4*mm* K_3TiOF_5 are shown in **Figure 8b**. (Note, we did not examine the dynamical stability of the commensurate phase directly owing to the computational expense for such a large cell.) The calculation shows 3 unstable optical branches that persist throughout the Brillouin zone between about 80*i* and 45*i* cm^{-1}. There are also unstable modes around the Σ point and between Γ → Z. We did not observe any instabilities between high symmetry points corresponding to our modulation vector, however this may be due to the limitations of our DFT calculation as we used the frozen phonon method which interpolates the bands between high-symmetry points compatible with our simulation cell. We are certain about which bands are unstable (see methods for convergence details) and that the acoustic-like mode instability from Γ → Z does not correspond to the commensurate structure. For example, the atomic displacements at **k** = (0,0,0.2) do not match those observed experimentally. The lower frequency unstable optical modes need further investigation to conclusively determine if they contribute to the displacive transition.

If no instabilities corresponding to the commensurate phase are found, there are two possible explanations for the lack of a soft mode within this displacive model: (i) the average commensurate structure, *I*4*mm*, is not the relevant parent structure for this analysis, thus, the calculated phonons of the commensurate structure are not expected to condense and give the commensurate phase; and (ii) the transition between the *I*4*mm* phase and the commensurate phase involves a significant order-disorder component and cannot be fully described with a displacive model. Based on the experimental commensurate structure, we may expect some order-disorder component to the phase transition owing to the significant orientational disorder of the Ti octahedra. Based on the orientations of the $[TiOF_5]^{3-}$ octahedra in the commensurate structure, it appears that the rotations of the Ti octahedra can be very large,

rotating up to (or more than) 90° largely about the *c*-axis. To compare the degree of order-disorder and displacive components of the phase transition, we next describe how the order-disorder component may be assessed computationally.

Order-disorder phase transitions are typically characterized by very low dispersion unstable bands that span the whole Brillouin zone. These flat bands may indicate that the phases along these paths have similar energy wells and low energetic barriers which allows the structure to hop among different states.[47,48] In the case of *I*4*mm*, there are unstable bands that span the whole Brillouin zone, but the bands have high and low dispersion regions. The low dispersion regions are shown in the lowest frequency band between Γ → X and the band around 80*i* cm^{-1} in the Γ → Z direction. We calculate the energy wells of the two phases connected by a phonon eigenvector and find that the wells are comparable; the energy minima differ by only 2 and 4 meV per formula unit for the low dispersion bands along Γ → X and Γ → Z, respectively. To further assess the order-disorder nature of the transition, the energetic barrier between these wells could be calculated, but is outside of the scope of this study. Further experimental investigations could also provide insight into the order-disorder component of the transition, either through high temperature structural characterization or through the measurement of ferroelectric properties, which could be used to determine the displacive degree of the transition through the Rhodes–Wohlfarth parameter.[49]

Although we do not know the exact mechanisms for the commensurate transition, the assembly of heteroleptic units in heteroanionic materials is very sensitive to the elemental properties of the counter-cations (e.g., ionic size, charge, polarizability)[6] and other commensurate structures with large unit cells have shown sensitivity to the choice of A-site cation.[14] Therefore, we next performed a computational experiment investigating the effect of changing the 6-fold coordinated B-site in the heteroanionic double perovskite. We substituted the K^+ ion in K_3TiOF_5 for the smaller Na^+ (1.02 Å) and larger Rb^+ (1.52 Å), relaxed the structures, and recomputed the phonon dispersions. **Figure 8** compares the phonon dispersions of the *I*4*mm*-type $K_2NaTiOF_5$ and $K_2RbTiOF_5$, respectively with K_3TiOF_5. The aforementioned acoustic instabilities between Γ → X and Γ → Σ in K_3TiOF_5 still appear with the substituted B sites, suggesting they play a similar role in the structure of all compounds. The unstable bands arising from optical branches, spanning the whole Brillouin zone in K_3TiOF_5, are hardened significantly in the Na-substituted compound, and are only slightly changed in the Rb-substituted compound. This dependence on A-cation chemistry suggests that the favorable bonding between Na-F originating from hard and soft acids and bases (HSAB) interactions influence the appearance of the soft modes. This could also originate from a chemical pressure effect from the A-site cation, as there is a large change in the volume between the three compounds (the volumes of the Na, K, and Rb compounds are 288 $Å^3$, 340 $Å^3$, and 369 $Å^3$, respectively). However, the relatively small changes in the frequencies of these bands between the K and Rb compounds, compared to the change from K to Na, suggest it may be driven by HSAB interactions along with size effects. Previous studies have noted the ability of Na^+ counter cations to direct the orientation of heteroleptic polyhedra through its preferred bonding to F^- in oxyfluorides.[13,50] Additionally, in other cryolite and elpasolite-type Ti oxyfluorides (**Table S3**), we find compounds with Na (e.g., $Cs_2NaTiOF_5$ and Na_3TiOF_5) adopt distorted structures rather than the aristotype cubic structure, meaning that their structural changes may be in part due to preferential Na-F bonding. Therefore, we posit that the commensurability may be more favorable in non-Na^+ containing Ti oxyfluorides.

Last, we probed the commensurate modulations effect on the electronic structure. Because calculation of the commensurate cell's electronic structure is unfeasible due to its large size, we instead calculated the electronic structures of two derivative phases obtained from modulating the lowest frequency phonon modes into the structure (**Figure S7**). We condensed the lowest frequency phonon mode on the *I*4*mm* structure (Figure S7d) to obtain the derivative monoclinic *Cm* structure (Figure S7e), which consists of $a^+a^+c^0$ octahedral tilts of the $[TiOF_5]^{3-}$ octahedra. We repeat this process again on the *Cm* structure to obtain the *Pc* structure (Figure S7f), which adds $a^0a^0c^+$ octahedral rotations of the $[TiOF_5]^{3-}$ into the structure. These modulations are consistent with the octahedral tilts and rotations observed in the commensurately modulated structure. Their densities of states as expected are quite similar to one another (Figure S7a,b,c). The band gap slightly widens with the distortions from 4.13 eV in the *I*4*mm* structure to 4.16 and 4.19 eV in the *Cm* and *Pc* structures, respectively. This is consistent with other perovskite-like heteroanionic materials which find a widening of the band gap with octahedral tilts and rotations.[51] The O 2*p* and F 2*p* states in the valence band change slightly, with the O 2*p* states and F 2*p* states around –3 to -3.5 eV and -1.5 to -2.2 eV separating into distinct bands, which is due to the change in orbital overlap with the octahedral rotations and tilts.

Conclusion

Single crystals of K_3TiOF_5 were obtained by a high temperature method and studied at 100 K via single-crystal X-ray diffraction. The atomic structure of K_3TiOF_5 is a commensurate superstructure of perovskite. Refinements showed that the subcell is pseudo-tetragonal with unit cell constants of $a = b = 6.066(2)$ Å and $c = 8.628(2)$ Å, and the length of the modulation vector is $0.3a^* + 0.1b^* + 0.25c^*$. The Ti^{4+} ions are significantly displaced from their average atomic positions (approximately of order ±0.13 Å) as refined in the subcell, while octahedrally coordinated K^+ ions were found to have large displacements of about ±0.76 Å. The IR and Raman spectra show only one Ti-O stretching vibration suggesting that all octahedrally coordinated Ti units were $[TiOF_5]^{3-}$. A marked decrease in $\nu_{Ti\text{-}O}$, compared with a previously reported value (from $\nu_{Ti\text{-}O}$ = 885 cm^{-1} to $\nu_{Ti\text{-}O}$ = 915 cm^{-1}) may be due to a weaker interaction of the *d*-*p* metal oxide π orbital owing to the large displacement of Ti from the average position in the crystal structure. S/TEM data indicated an average structure that matched well with the idealized anion-ordered *I*4*mm* lattice. One- and two-dimensional solid-state ^{19}F NMR measurements further confirmed the ordered anion sublattice with two sets of resonances corresponding to axial and equatorial fluorine in the $[TiOF_5]^{3-}$ unit. The commensurate structure of K_3TiOF_5 was attributed to a combination of a displacive and order-disorder phase transitions, whose quantitative contributions open a direction for future exploration. DFT calculations indicate that the instability of soft optical modes is correlated with both the size of

the *B*-site cations and HSAB interactions, which suggests that the presence of octahedrally coordinated K^+ ions also play a role in the commensurability of K_3TiOF_5.

ASSOCIATED CONTENT

Supporting Information

Experimental and calculated XRD patterns, DTA curves, single crystal photo, SAED figure, SHG measurements of powdered K_3TiOF_5 crystals, additional crystallographic details, Fourier components of the displacive modulation, DOS and atomic structures of derivative phonon-modulated phases.

CCDC 2085578 contains the supplementary crystallographic data for this paper. These data can be obtained free of charge via www.ccdc.cam.ac.uk/data_request/cif, or by emailing data_request@ccdc.cam.ac.uk, or by contacting The Cambridge Crystallographic Data Centre, 12 Union Road, Cambridge CB2 1EZ, UK; fax: +44 1223 336033.

AUTHOR INFORMATION

Corresponding Author

James M. Rondinelli: jrondinelli@northwestern.edu

Kenneth R. Poeppelmeier: krp@northwestern.edu

Notes

The authors declare no competing financial interest.

[1]F.D and N.C. contributed equally.

ACKNOWLEDGMENT

F.D., C.D.M. and M.L.N. were supported by funding from the National Science Foundation (DMR-1904701) for the single crystal XRD work. NMR studies performed by K.J.G were supported by the Joint Center for Energy Storage Research (JCESR), an Energy Innovation Hub funded by the U.S. Department of Energy, Office of Science, Office of Basic Energy Sciences. Theoretical and computational work of J.K.H., N.C. and J.M.R. were supported by NSF (DMR-1454688 and DMR-2011208). W.G. and P.S.H. thank the Welch Foundation (Grant E-1457) for support. Experimental synthesis and structure characterization by J.K.H., C.Z., K.R.P., J.M.R. and V.P.D. were supported by the National Science Foundation's (NSF) MRSEC program (DMR-1720139) at the Materials Research Center of Northwestern University. The single-crystal X-ray data, NMR, and FT-IR measurements were acquired at Northwestern University's Integrated Molecular Structure Education and Research Center (IMSERC) at Northwestern University, which is supported by grants from NSF-NSEC, NSF-MRSEC, the KECK Foundation, the Soft and Hybrid Nanotechnology Experimental (SHyNE) Resource (NSF ECCS-2025633), the State of Illinois, and Northwestern University. This work made use of the J. B. Cohen X-ray Diffraction Facility supported by the MRSEC program of the National Science Foundation (DMR-1720139) at the Materials Research Center of Northwestern University. DFT calculations were performed on the high-performance computing facilities available at the Extreme Science and Engineering Discovery Environment (XSEDE), which was supported by NSF Grant No. ACI-1548562.

REFERENCES

1. Pauling, L., The crystal structures of ammonium fluoferrate, fluoaluminate and oxyfluomolybdate. *J. Am. Chem. Soc.* **1924,** *46*, 2738-2751.
2. Katsumata, T.; Nakashima, M.; Umemoto, H.; Inaguma, Y., Synthesis of the novel perovskite-type oxyfluoride PbScO2F under high pressure and high temperature. *J. Solid State Chem.* **2008,** *181*, 2737-2740.
3. Hartman, S. T.; Cho, S. B.; Mishra, R., Multiferroism in iron-based oxyfluoride perovskites. *Inorg. Chem.* **2018,** *57*, 10616-10624.
4. Harada, J. K.; Poeppelmeier, K. R.; Rondinelli, J. M., Predicting the Structure Stability of Layered Heteroanionic Materials Exhibiting Anion Order. *Inorg. Chem.* **2019,** *58*, 13229-13240.
5. Kageyama, H.; Hayashi, K.; Maeda, K.; Attfield, J. P.; Hiroi, Z.; Rondinelli, J. M.; Poeppelmeier, K. R., Expanding frontiers in materials chemistry and physics with multiple anions. *Nat. Commun.* **2018,** *9*, 772.
6. Harada, J. K.; Charles, N.; Poeppelmeier, K. R.; Rondinelli, J. M., Heteroanionic Materials by Design: Progress Toward Targeted Properties. *Adv. Mater.* **2019,** *31*, 1805295.
7. Chaminade, J. P.; Cervera-Marzal, M.; Ravez, J.; Hagenmuller, P., Ferroelastic and ferroelectric behavior of the oxyfluoride $Na_3MoO_3F_3$. *Mater. Res. Bull.* **1986,** *21*, 1209-1214.
8. Peraudeau, G.; Ravez, J.; Tressaud, A.; Hagenmuller, P.; Arend, H.; Chanussot, G., Les transitions de phase de l'oxyfluorure $Rb_3MoO_3F_3$. *Solid State Commun.* **1977,** *23*, 543-546.
9. Peraudeau, G.; Ravez, J.; Hagenmuller, P.; Arend, H., Study of phase transitions in $A_3MO_3F_3$ compounds (A= K, Rb, Cs; M= Mo, W). *Solid State Commun.* **1978,** *27*, 591-593.
10. Ravez, J.; Peraudeau, G.; Arend, H.; Abrahams, S.; Hagenmuller, P., A new family of ferroelectric materials with composition $A_2BMO_3F_3$ (A, B= K, Rb, Cs, for rA+⩾ rB+ and M= Mo, W). *Ferroelectrics.* **1980,** *26*, 767-769.
11. Ye, Z. G.; Ravez, J.; Rivera, J. P.; Chaminade, J.P.; Schmid, H., Optical and dielectric studies on ferroelectric oxyfluoride $K_3MoO_3F_3$ single crystals. *Ferroelectrics.* **1991,** *124*, 281-286.
12. Brink, F.; Noren, L.; Goossens, D.; Withers, R.; Yun, L.; Xu, C., A combined diffraction (XRD, electron and neutron) and electrical study of $Na_3MoO_3F_3$. *J. Solid State Chem.* **2003,** *174*, 450-458.
13. Fry, A. M.; Seibel, H. A.; Lokuhewa, I. N.; Woodward, P. M., $Na_{1.5}Ag_{1.5}MO_3F_3$ (M= Mo, W): An Ordered Oxyfluoride Derivative of the $LiNbO_3$ Structure. *J. Am. Chem. Soc.* **2012,** *134*, 2621-2625.
14. Fry, A. M.; Woodward, P. M., Structures of α-$K_3MoO_3F_3$ and α-$Rb_3MoO_3F_3$: ferroelectricity from anion ordering and noncooperative octahedral tilting. *Cryst. Growth Des.* **2013,** *13*, 5404-5410.
15. Pausewang, G.; Rüdorff, W., Über Alkali-oxofluorometallate der Übergangsmetalle. A MeO_xF_{6-x}-Verbindungen mit x= 1, 2, 3. *Z. Anorg. Allg. Chem.* **1969,** *364*, 69-87.
16. Sheng, J.; Tang, K.; Cheng, W.; Wang, J.; Nie, Y.; Yang, Q., Controllable solvothermal synthesis and photocatalytic properties of complex (oxy) fluorides K_2TiOF_4, K_3TiOF_5, $K_7Ti_4O_4F_7$ and K_2TiF_6. *J. Hazard. Mater.* **2009,** *171*, 279-287.
17. Zhang, B.; Lu, L.; Lai, M.; Fang, H.; Ma, H.; Li, J., Synthesis mechanism of an Al-Ti-C grain refiner master alloy prepared by a new method. *Metall. Mater. Trans. A* **2003,** *34*, 1727-1733.

18. Fouad, M.; Chaminade, J.; Ravez, J.; Sadel, A. In *Ferroelastic Domain Study in Crystals with Formula K_3TiOF_5, $K_3MO_2F_4$ and $K_3M'O_3F_3$ (M= Nb, Ta; M'= Mo, W)*, Advanced Materials Research, Trans Tech Publ: 1994; pp 469-478.
19. Beckmann, P. A.; Dybowski, C., A thermometer for nonspinning solid-state NMR spectroscopy. *Journal of magnetic resonance (San Diego, Calif.: 1997)* **2000,** *146*, 379-380.
20. Bielecki, A.; Burum, D. P., Temperature dependence of ^{207}Pb MAS spectra of solid lead nitrate. an accurate, sensitive thermometer for variable-temperature MAS. *Journal of Magnetic Resonance, Series A* **1995,** *116*, 215-220.
21. *Bruker. APEX2 Version 2009.5-1 and SAINT Version 7.34a Data Collection and Processing Software*. Bruker Analytical X-Ray Instruments, Inc.: Madison, WI, USA: 2009.
22. Sheldrick, G. M., A short history of SHELX. *Acta Crystallogr. Sect. A: Found. Crystallogr.* **2008,** *64*, 112-122.
23. Petricek, V.; Dusek, M.; Palatinus, L. *Jana 2006*, Institute of Physics: Praha, Czech Republic, 2006.
24. Oszlányi, G.; Sütő, A., Ab initio structure solution by charge flipping. *Acta Crystallogr. Sect. A* **2004,** *60*, 134-141.
25. Oszlányi, G.; Sütő, A., Ab initio structure solution by charge flipping. II. Use of weak reflections. *Acta Crystallogr. Sect. A* **2005,** *61*, 147-152.
26. Kresse, G.; Furthmüller, J., Efficient iterative schemes for ab initio total-energy calculations using a plane-wave basis set. *Phys. Rev. B* **1996,** *54*, 11169.
27. Kresse, G.; Furthmüller, J., Efficiency of ab-initio total energy calculations for metals and semiconductors using a plane-wave basis set. *Comput. Mater. Sci.* **1996,** *6*, 15-50.
28. Perdew, J. P.; Ruzsinszky, A.; Csonka, G. I.; Vydrov, O. A.; Scuseria, G. E.; Constantin, L. A.; Zhou, X.; Burke, K., Restoring the density-gradient expansion for exchange in solids and surfaces. *Phys. Rev. Lett.* **2008,** *100*, 136406.
29. Charles, N.; Rondinelli, J. M., Assessing exchange-correlation functional performance for structure and property predictions of oxyfluoride compounds from first principles. *Phys. Rev. B* **2016,** *94*, 174108.
30. Blöchl, P. E., Projector augmented-wave method. *Phys. Rev. B* **1994,** *50*, 17953.
31. Monkhorst, H. J.; Pack, J. D., Special points for Brillouin-zone integrations. *Phys. Rev. B* **1976,** *13*, 5188.
32. Togo, A.; Tanaka, I., First principles phonon calculations in materials science. *Scr. Mater.* **2015,** *108*, 1-5.
33. Stokes, H.; Hatch, D.; Campbell, B., Isotropy software suite. *URL* https://stokes.byu.edu/iso/isotropy.php **2017**.
34. Stokes, H. T.; Campbell, B. J.; Hatch, D. M., Order parameters for phase transitions to structures with one-dimensional incommensurate modulations. *Acta Crystallogr. A* **2007,** *63*, 365-373.
35. Du, L. S.; Schurko, R. W.; Kim, N.; Grey, C. P., Solid-state ^{93}Nb, ^{19}F, and ^{113}Cd nuclear magnetic resonance study of niobium oxyfluorides: characterization of local distortions and oxygen/fluorine ordering. *J. Phys. Chem. A* **2002,** *106*, 7876-7886.
36. Šimko, F. e.; Rakhmatullin, A.; Véron, E.; Allix, M.; Florian, P.; Kontrík, M.; Netriová, Z.; Korenko, M.; Kavečanský, V.; Bessada, C., Oxo-and Oxofluoroaluminates in the RbF–Al_2O_3 System: Synthesis and Structural Characterization. *Inorg. Chem.* **2018,** *57*, 13702-13712.
37. Flynn, S.; Zhang, C.; Griffith, K. J.; Shen, J.; Wolverton, C.; Dravid, V. P.; Poeppelmeier, K. R., Fluoridation of HfO_2. *Inorg. Chem.* **2021,** *60*, 4463-4474.
38. Kunz, M.; Brown, I. D., Out-of-center distortions around octahedrally coordinated d0 transition metals. *J. Solid State Chem.* **1995,** *115*, 395-406.
39. Voit, E.; Davydov, V.; Mashkovskii, A.; Voit, A., Investigation of oxofluorotitanates $(NH_4)_3TiOF_5$ and Rb_2KTiOF_5 by vibrational spectroscopy and quantum-chemical methods. *J. Struct. Chem.* **2008,** *49*, 13-20.
40. Dvorak, V.; Petzelt, J., Infrared and Raman activity of soft modes in the incommensurate structure. *J. Phys. C* **1978,** *11*, 4827.
41. Krylov, A.; Goryainov, S.; Vtyurin, A.; Krylova, S.; Sofronova, S.; Laptash, N.; Emelina, T.; Voronov, V.; Babushkin, S., Raman scattering study of temperature and hydrostatic pressure phase transitions in Rb_2KTiOF_5 crystal. *J. Raman Spectrosc.* **2012,** *43*, 577-582.
42. Udovenko, A. A.; Laptash, N. M., Dynamic orientational disorder in crystals of fluoroelpasolites, structural refinement of $(NH_4)_3AlF_6$,$(NH_4)_3TiOF_5$ and Rb_2KTiOF_5. *Acta Cryst. B* **2011,** *67*, 447-454.
43. Ding, F.; Griffith, K. J.; Koçer, C. P.; Saballos, R. J.; Wang, Y.; Zhang, C.; Nisbet, M. L.; Morris, A. J.; Rondinelli, J. M.; Poeppelmeier, K. R., Multimodal Structure Solution with ^{19}F NMR Crystallography of Spin Singlet Molybdenum Oxyfluorides. *J. Am. Chem. Soc.***2020,** *142*, 12288-12298.
44. Ramsey, N. F., Magnetic shielding of nuclei in molecules. *Phys. Rev.* **1950,** *78*, 699.
45. Ramsey, N. F., Chemical effects in nuclear magnetic resonance and in diamagnetic susceptibility. *Physical Review* **1952,** *86*, 243.
46. Saika, A.; Slichter, C., A note on the fluorine resonance shifts. *J. Chem. Phys.* **1954,** *22*, 26-28.
47. Xu, B.; Hellman, O.; Bellaiche, L., Order-disorder transition in the prototypical antiferroelectric $PbZrO_3$. *Phys. Rev. B* **2019,** *100*, 020102.
48. Skjærvø, S. H.; Meier, Q. N.; Feygenson, M.; Spaldin, N. A.; Billinge, S. J.; Bozin, E. S.; Selbach, S. M., Unconventional continuous structural disorder at the order-disorder phase transition in the hexagonal manganites. *Phys. Rev. X* **2019,** *9*, 031001.
49. Perez-Mato, J.; Etxebarria, I.; Radescu, S.; Ivantchev, S., The Rhodes-Wohlfarth parameter as assessment of the displacive degree in ferroelectrics: The case of the Φ 4> model. *Eur. Phys. J. B* **1999,** *12*, 331-334.
50. Donakowski, M. D.; Vinokur, A. I.; Poeppelmeier, K. R., The Dimeric $[V_2O_4F_6]^{4-}$Vanadium Oxide-Fluoride Anion in $Na_2(M(H_2O)_2)(V_2O_4F_6)$(M= Co^{2+}, Ni^{2+}, and Cu^{2+}). *Z. Anorg. Allg. Chem.* **2012,** *638*, 1991-1995.
51. Vonrüti, N.; Aschauer, U., Epitaxial strain dependence of band gaps in perovskite oxynitrides compared to perovskite oxides. *Phys. Rev. Mater.* **2018,** *2*, 105401.

Insert Table of Contents artwork here

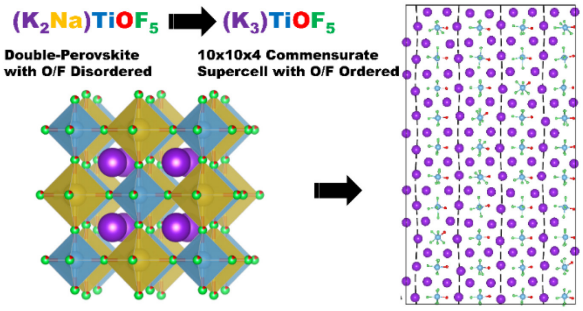
(K2Na)TiOF5
(K3)TiOF5
Double-Perovskite
with O/F Disordered
10x10x4 Commensurate
Supercell with O/F Ordered